Effect of dynamic formation of multiphase slag skin on heat transfer and magneto-hydrodynamic flow in electroslag remelting process

Wang, Fang; Tan, Jianpeng; Liu, Zhongqiu; Baleta, Jakov; Li, Baokuan

Source / Izvornik: **Journal of Materials Research and Technology, 2023, 25, 1696 - 1708**

Journal article, Published version
Rad u časopisu, Objavljena verzija rada (izdavačev PDF)

https://doi.org/10.1016/j.jmrt.2023.06.042

Permanent link / Trajna poveznica: https://urn.nsk.hr/urn:nbn:hr:115:275185

Available online at www.sciencedirect.com

jmr&t Journal of Materials Research and Technology

journal homepage: www.elsevier.com/locate/jmrt

Effect of dynamic formation of multiphase slag skin on heat transfer and magneto-hydrodynamic flow in electroslag remelting process

Fang Wang [a,b,*], *Jianpeng Tan* [b], *Zhongqiu Liu* [b,**], *Jakov Baleta* [c], *Baokuan Li* [b]

[a] *Key Laboratory for Ecological Metallurgy of Multimetallic Ores (Ministry of Education), Northeastern University, Shenyang, 110819, China*

[b] *School of Metallurgy, Northeastern University, Shenyang, 110819, China*

[c] *Faculty of Metallurgy, University of Zagreb, Sisak, 44 103, Croatia*

ARTICLE INFO

Article history:
Received 19 April 2023
Accepted 5 June 2023
Available online 8 June 2023

Keywords:
Electroslag remelting process
Formation of slag skin
Heat transfer
Melting

ABSTRACT

During the electroslag remelting (ESR) process, the effect of dynamic formation of slag skin on magneto-hydrodynamic multiphase flow and temperature field is studied using a 2-D axisymmetric model. The electromagnetic field is described by user-defined functions. The dynamic formation and distribution of multiphase slag skin, as well as the interface between slag and metal, are investigated by using the volume of fluid (VOF) model and the dynamic meshing method. Especially, the effect of slag skin/air gap on heat transfer characteristics is considered and developed by user-defined functions. The results show that the thickness of slag skin at the interface between slag and metal increases as the axial distance from free surface of slag rises, reaching a maximum of about 25 mm. With the height of ingot increasing, the thickness of slag skin drops to 17 mm. When the current changes from 2.0 kA to 3.0 KA in the ESR process, the current density, Joule heat, velocity and temperature increases. In the meanwhile, the slag skin becomes thinner and the melt pool becomes deeper. The vibration of electrode has a weak effect on the formation behavior of slag skin, and only has effects on formation of metal droplet and velocity field.

1. Introduction

With the rapid development of modern aviation industry, the main hot end drive devices of engines, such as the high temperature alloy turbine discs and high pressure compressor discs, are required to improve the mechanical properties. The GH4065A alloy is used as the key high temperature turbine disc material [1–4]. To meet the growing demand for high-quality alloy, the electroslag remelting (ESR) technology offers a substantial improvement in serviceability and working life. As seen in Fig. 1, when an alternating current (AC) is conveyed from the electrode to bottom, the Joule heating of slag generates during the ESR process. A liquid metal pool forms in the water-cooled mold where the dense metal droplets penetrate the less dense slag [5]. As the metal

* Corresponding author.
** Corresponding author.
E-mail addresses: wangfang@smm.neu.edu.cn (F. Wang), liuzq@smm.neu.edu.cn (Z. Liu).
https://doi.org/10.1016/j.jmrt.2023.06.042

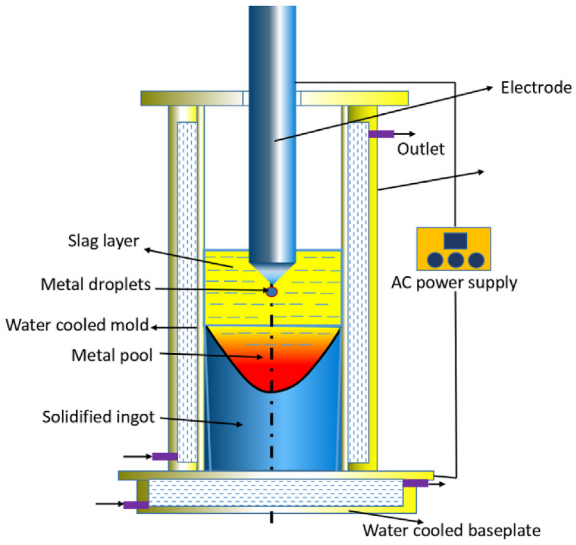

Fig. 1 – Schematic diagram of eletroslag remelting process.

droplets fall, the chemical refining occurs in the slag. The liquid metal is solidified to the ingot in mold, which is cooled by water.

The common ingot defects in the ESR process are internal and surface defects [6,7]. Internal defects of ingots are primarily caused by coarsening, segregation, and fracturing of grain. The irregular temperature distribution of ingot frequently leads to the formation of surface defects, including uneven surface and fissures. To control surface defects of ingots, it is essential to comprehend that how slag skin dynamically forms.

As the remelting proceeds, the liquid slag solidifies due to the cooling water, the solidified slag skin is generated near the mold wall [8,9]. Normally, the ingot has a smooth surface. Particularly, the ingots with thicker skin may become surface defects, resulting in significant grinding losses. The traditional methods for reducing surface defects are including increasing the temperature of mold, reducing the remelting voltage, and increasing the distance between electrodes and walls [10]. However, there are many disadvantages such as high cost, difficulty, and furnace type requirements in the traditional methods. The different types of slag skin also have different heat transfer characteristics [11–13]. The investigation of dynamic formation process of multi-phase slag layers is essential for the control of surface defects.

The slag skin is not made of only single component, but a variety of components [8]. The components in slag skin show a chaotic layering phenomenon according to melting temperature of slag skin, and the components which has high melting temperature is firstly precipitated during solidification. The slag skin layering phenomenon (a) only one layer slag skin and (b) three-phase slag skin is shown in Fig. 2. As shown in Fig. 2(b), from the left to the right, the solid slag layer near the mold is named $Slag_1$, whose component is only Al_2O_3. The solid slag layer in the middle is named $Slag_2$, whose component is a mixture of Al_2O_3 and CaF_2. The solid slag next to the middle slag layer is named $Slag_3$, whose component is only CaF_2. The content of Al and O in slag increases and then decreases. While on the contrary, the content of F and Ca in slag demonstrates oppositely.

Some efforts have been made to numerically analysis the effect of slag skin on electromagnetic field, two-phase flow and temperature distribution in the ESR process. Hugo et al. [14] employed a 2-D symmetric transient model to find out the influence of slag skin on current for different parameters. Yanke et al. [15] explored the effect of mold diameter and current on slag skin development by modeling formation of slag skin. Yu et al. [16] studied the impact of development and dispersion of heat flow on slag skin during the ESR process. Kharicha et al. [17] simulated the formation of slag skin only in slag pool with and without conductive mold during electroslag remelting process. There are other experiment studies on the ESR investigations. Meng et al. [18] concluded that the stratification phenomenon in the formation of slag skin exists and the slag skin composition are given by experiments. Li et al. [19] investigated the solidification mechanism of slag skins at different stages of physical and compositional changes. The stratification phenomena and the composition of slag skin produced by the chill layer were investigated by Zhao et al. [20]. Chu et al. [21] hypothesized the presence of a "small annular molten pool" at the top perimeter based on a petrographic analysis of slag skin with a tiny ESR ingot. Still, relatively little is known about the slag skin/air gap heat transfer mechanism. Little attempts have been conducted on the slag/air gap heat transfer mechanism and the delamination of slag skin.

As discussed above, the formation of slag skin during the ESR process remains unclear, especially for the multiphase slag skin. In this study, the authors establishes a multi-physical field mathematical model considering heat transfer characteristics of slag skin/air gap to numerically clarify the formation of slag skin coupled with magneto-hydrodynamic multi-phase flow and temperature fields. The effect of current and vibrating electrode on slag skin solidification behavior were investigated. The experimental and the simulation results were compared for the validation of model.

2. Model description

2.1. Assumptions

The model is based on the following assumptions to make the computing reasonably.

(1) The domain contains liquid slag, solid slag skin and metal.
(2) The electrode tip is flat.
(3) The solidification process ignores shrinkage.
(4) Assuming that the physical characteristics of metal and slag remain unchanged.

2.2. Electromagnetism

In the ESR process, the AC is used, so the electromagnetic field is described by Maxwell equations [22].

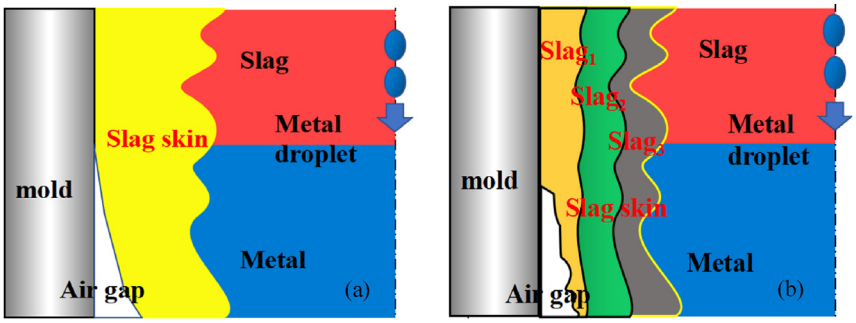

Fig. 2 – Slag skin layering phenomenon (a) only one layer slag skin and (b) three-phase slag skin.

$$\nabla \cdot \vec{J} = 0 \tag{1}$$

$$\vec{J} = -\sigma \frac{\partial \vec{A}}{\partial t} - \sigma \nabla \varphi \tag{2}$$

$$\nabla \times \vec{H} = \vec{J} \tag{3}$$

$$\vec{B} = \nabla \times \vec{A} = \mu_0 \vec{H} \tag{4}$$

The electromagnetic force $\vec{F_c}$ and Joule heat Q_J distribution are listed as follows:

$$\vec{F_c} = \vec{J} \times \vec{B} \tag{5}$$

$$Q_J = \frac{\vec{J} \cdot \vec{J}}{\sigma} \tag{6}$$

where: $\vec{J}$ is the current density; σ is the conductivity of magnetic fluid; $\vec{A}$ is the magnetic potential vector; t is time; φ is the electric potential; $\vec{H}$ is the magnetic field; $\vec{B}$ is the magnetic flux density; μ_0 is the magnetic permeability of medium; $\vec{F_c}$ is the electromagnetic force; Q_J is Joule heat.

The multiphase flow of slag and liquid metal is described by the VOF model. The turbulent effects are solved by the RNG model, which has an enhanced wall function in the near-wall region. The VOF method is used to trace the interface between molten alloy and slag [23]:

$$\frac{\partial \alpha_i}{\partial t} + \nabla(v\alpha_i) = 0 \tag{7}$$

where: α_i is the volume fractions. The subscript "i" represents the type of substance, including metal(m), liquid slag(s), solid $slag_1$(s1),solid $slag_2$(s2) and solid $slag_3$(s3), respectively. All the combination of volume fractions are equal to 1, as shown in Eq. (8):

$$\sum_{i=1}^{n_{phases}} \alpha_m + \alpha_s + \alpha_{s1} + \alpha_{s2} + \alpha_{s3} = 1 \tag{8}$$

The density, viscosity, and conductivity in other mixed phase characteristics, can be stated as:

$$\overline{\varphi} = \varphi_m \alpha_m + \varphi_s \alpha_s + \varphi_{s1} \alpha_{s1} + \varphi_{s2} \alpha_{s2} + \varphi_{s3} \alpha_{s3} \tag{9}$$

where: α_i is the volume fractions, $\overline{\varphi}$ is the mixed-phase parameter. The subscripts here have the same meaning as above.

2.3. *Fluid flow*

The flow of liquid slag and liquid metal are modeled during the ESR process. The conservation of mass and momentum are solved to determine the velocity field [24].

$$\partial \rho_{mix} / \partial t + \nabla \cdot (\rho_{mix} \vec{v}) = 0 \tag{10}$$

$$\partial(\rho_{mix} \vec{v}) / \partial t + \nabla \cdot (\rho_{mix} \vec{v} \times \vec{v}) = -\nabla p + \nabla\left(\mu_{eff} \cdot \nabla \vec{v}\right) + \vec{F}_{st} + \vec{F}_e + \vec{F}_d + \vec{F}_t \tag{11}$$

where: μ_{eff} is determined by Eq. (12); ρ_{mix} is the density of the mixed-phase; F_{st} is the surface tension between the slag and alloy phases; F_e is the Lorentz force; F_d is the paste zone resistance; F_t is the thermal buoyancy force due to the density difference.

$$\mu_{eff} = \mu + \rho_{mix} C_\mu \frac{k^2}{\varepsilon} \tag{12}$$

where: μ is the laminar viscosity; C_μ is constant; k is the turbulent kinetic energy; ε is the dissipation rate.

2.4. *Heat transfer*

The distribution of temperature is specified by the energy conservation Eq. (13). The only heat source in the ESR process is Joule heating, and the effective thermal conductivity is defined by the influence of turbulence. The solidification process of ingot is also considered in this paper [25].

$$\frac{\partial}{\partial t}(\rho_{mix} E) + \nabla \cdot (\vec{v} \rho_{mix} E) = \nabla \cdot \left(k_{eff} \nabla T\right) + Q_J \tag{13}$$

where: ρ_{mix} is the density of the mixed-phase; E is the internal energy; k_{eff} is the effective thermal conductivity, which can be calculated by the following equation:

$$k_{eff} = b c_p \mu_{eff} \tag{14}$$

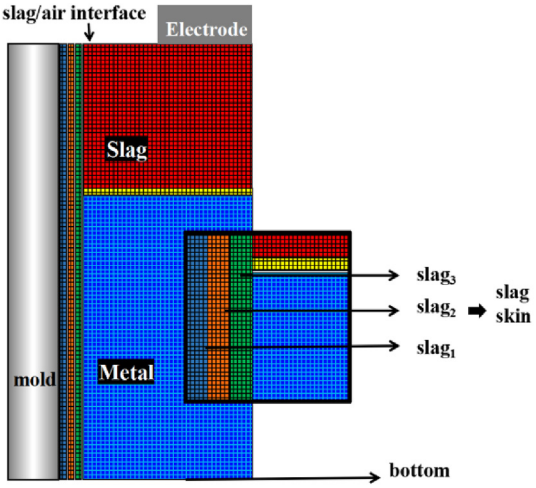

Fig. 3 – Schematic diagram of computational domain.

where: b is the reciprocal of Prandtl Number; c_p is the specific heat capacity obtained by Eq. (15); E is the internal energy of the mixed-phase concerning latent heat and temperature [26]:

$$E = \frac{\left|\alpha_m \rho_m c_{p,m} + \overline{\alpha_s \rho_s c_{p,s}}\right|}{\alpha_m \rho_m + \overline{\alpha_s \rho_s}\, T} \tag{15}$$

$$\overline{c_{p,s}} = \alpha_s c_{p,s} + \alpha_{s1} c_{p,s1} + \alpha_{s2} c_{p,s2} + \alpha_{s3} c_{p,s3} \tag{16}$$

where: $c_{p,m}$ and $c_{p,s}$ denote the specific heat capacities of the metal and mixed-slag phases(mixture of four phase slag), respectively. ρ_m is the densities of metal. $\overline{\rho_s}$ is the densities of mixed-slag phases, which is defined by Eq. (9).

The enthalpy-porous medium model is utilized to calculate the solidification process, the mushy zone is considered as a porous medium. As the liquid metal solidifies, the porosity decreases from 1 to 0 progressively. f_1 is the resistance of the mushy zone. S_t in Eq. (18) is the source term for solving the latent heat of solidification, and the solution is as follows [27]:

$$\overrightarrow{F_t} = \frac{(1-f_1)^2}{f_1^3} A_{mush}(v - v_{cast}) \tag{17}$$

$$S_t = -\frac{\partial}{\partial t}(\rho_{mix} f_1 L) \tag{18}$$

where: v_{cast} is the casting velocity; f_1 is the liquid phase fraction; L is the latent heat of melting; A_{mush} is the paste zone coefficient. To ensure the stability of the calculation, the following formula is used to determine the distribution of liquid phase fraction f_1 [28]:

$$f_1 = \frac{T - T_S}{T_1 - T_S} \tag{19}$$

where: T_1 and T_s are the liquid and solid phase line temperatures of the metal, respectively.

2.5. Boundary conditions

The potential equation at the wall is as follows [29].

$$\text{Bottom:} \quad A_x = A_y = \frac{\partial A_z}{\partial z} = 0 \tag{20}$$

$$\text{Wall:} \quad A_x = A_y = A_z = 0 \tag{21}$$

Additionally, a no-slip condition is imposed on the wall. The Zero shear stress is applied on the top surface of the slag. The vibration of electrode is fixed on the inlet [30].

The metal with a velocity inlet at the electrode tip has a temperature of 1800 K. It is a challenge to estimate the heat exchange between slag and mold or between metal and mold due to slag solidification and air gap. Using the thermal convection with the equivalent heat transfer coefficient, the complex heat transfer phenomena between the metal and water-cooled mold are accounted for.

$$h = \frac{1}{\delta_s/k_s + 1/(h_r + h_c) + \delta_m/k_m + 1/h_w + R_{contact}} \tag{22}$$

where, δ_s is the slag skin thickness. k_s is the thermal conductivity of slag skin. h_r and h_c are the radiative and convective heat transfer factors of air gap, respectively. δ_m is the thickness of mold. k_m is the heat conductivity of mold. h_w is the total coefficient of heat transmission between the mold and the water for cooling, $R_{contact}$ is the contact resistance [31,32].

2.6. Numerical treatment

In this paper, the discrete equations are solved using the commercial software ANSYS-FLUENT 19.2. The calculation domain is divided into three regions, as depicted in Fig. 3. In the calculation domain, the zone of air gap is omitted, however, the thermal resistance of air gap is considered in the simulation. By means of user-defined functions, the

Table 1 – Physical properties of slag and metal.

Parameter	Value				
	Slag	Metal	$Slag_1$	$Slag_2$	$Slag_3$
Density, kg/m^3	2800	8280	2700	2900	2850
Dynamic viscosity, Pa s	0.02	0.006	0.02	0.02	0.02
Latent heat, kJ/kg	470	271	470	470	470
Specific heat, J/kg K	1255	752	1255	1255	1255
Electrical conductivity, S/m	216(L)/4(S)	111,000	201(L)/4(S)	182(L)/4(S)	161(L)/4(S)
Liquidus temperature(L), K	1620	1623	1580	1490	1460
Solidus temperature(S), K	1570	1448	1270	1280	1320

Table 2 – Process parameters and operating conditions.

Parameter	Value
Geometry parameters	
Electrode radius, mm	225
Mold radius, mm	250
Slag thickness, mm	310
Slag pool height, mm	50/40/30
Metal pool height, mm	30
δ_s (slag skin thickness), mm	20
δ_m (mold thickness), mm	30
Heat transfer at melt/mold, W/(m^2·K)	400
Heat transfer at bottom, W/(m^2·K)	400
Heat transfer at slag/air surface, W/(m^2·K)	80
Emissivity of slag at slag/air surface, W/(m^2·K)	0.6
Operating conditions	
Power, kW	110
Current Frequency, Hz	50

electromagnetic field, Joule heating, Lorentz force, and boundary conditions are described. The mixed heat exchange, including the natural convection (slag/air)and the radiation (slag/air)and the convective heat transfer (slag/electrode and slag/mold), are considered in the ESR. The growth rate of solidified ingot is determined by the inlet melt rate. The formation and distribution of multiphase slag skin are studied using the VOF model and dynamic meshing technique. The development of ingot is depicted using a dynamic meshing technique with hierarchical grid.

A 2D model was established in the study. The minimum mesh size of 1 mm and the maximum mesh size of 3 mm were employed in the domain. It is accord with grid independence. The maximum time step is 1×10^{-4} s. The calculation of simulation were performed on the Dell computing station sever (64 × 2.5 GHz-128GB). The initial calculation domain includes solid slag, liquid slag and metal. In addition, the temperature of mold is 500 K, and an initial slag layer of 20 mm thickness was applied. Approximately 60,000 structured meshes were generated for the entire computational domain. In Table 1, the physical properties of slag and metal were selected based on the experimental material [7,33] and reference [24,34]. Table 2 displays the geometry of model and the process parameters used in the ESR process. The

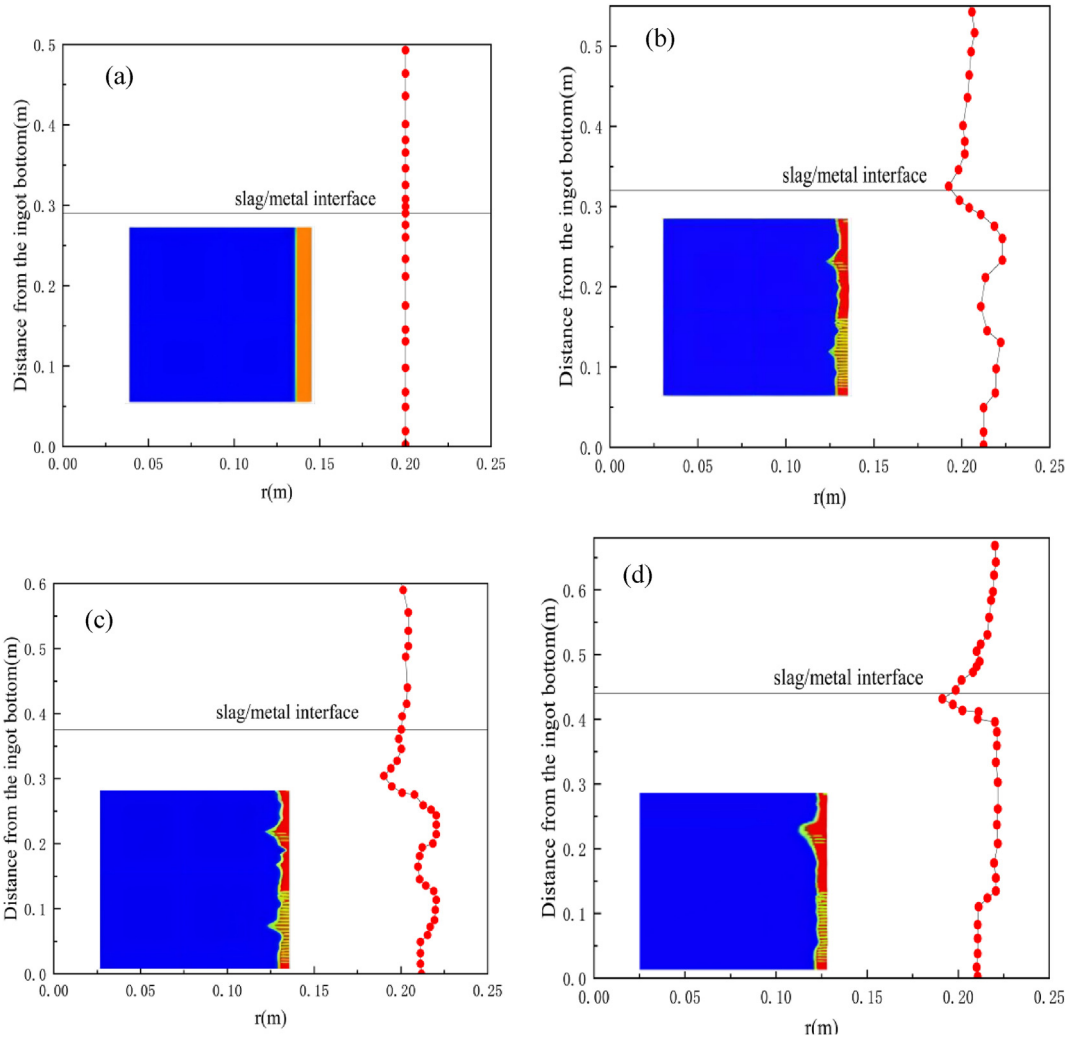

Fig. 4 – Variation of the thickness of slag skin versus time (a) t = 0s, (b) t = 30s, (c) t = 90s and (d) t = 150s.

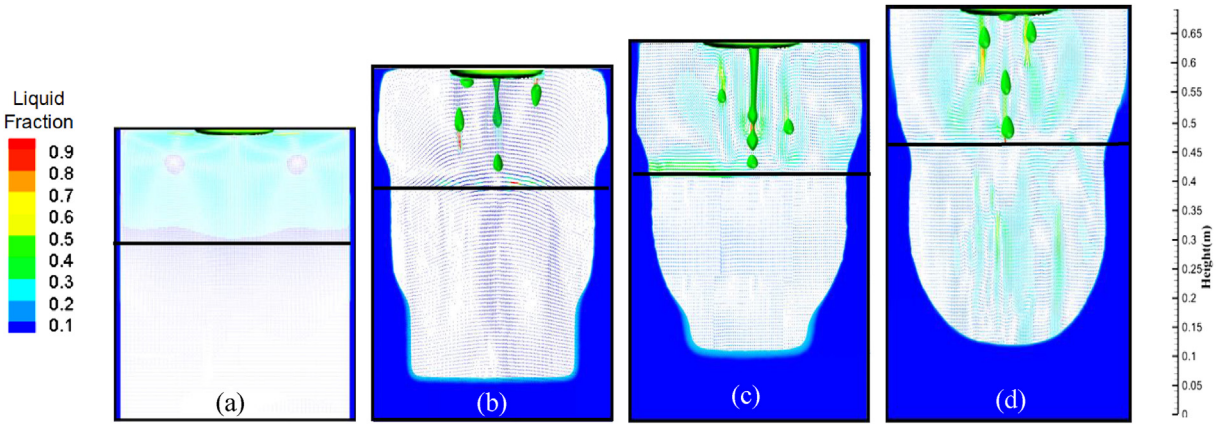

Fig. 5 – Variation of shape of melt pool profile versus time (a) t = 0s, (b) t = 30s, (c) t = 90s and (d) t = 150s.

interfacial tension between slag and metal is 0.90 N/m, and the surface emissivity of free slag is 0.60.

3. Results and discussion

3.1. *Slag skin solidification behavior*

As shown in Fig. 4, it is assumed that a 20 mm thick slag skin solidifies near the mold when t = 0 s. Under the action of water cooling on the mold wall, the slag near the slag skin began to solidify, resulting in an increase in the thickness of the slag skin. At t = 30s, the slag skin at the slag skin/molten metal interface contacts the molten metal in the metal molten pool, and the increased overheating part melts the slag skin, resulting in a decrease in the thickness of the slag skin in this part. Under the strong water cooling, the thickness of the slag skin contacting the slag will slowly increase above the slag skin/molten metal interface, eventually reaching 24 mm, forming a curved crescent shape. As the remelting process progresses, the temperature in the slag pool increases, and the slag skin contacting the metal continues to melt at a higher temperature. The thickness of slag at the slag skin/metal interface continues to thin. At t = 90 s, the thickness of the slag skin in contact with the molten metal becomes thinner and thinner, which is due to the temperature in the slag pool increases. And the slag skin in contact with the molten slag becomes thinner, down to only 21 mm. At t = 150 s, as the ESR process proceeds, the temperature in the slag pool increases. The thickness of the slag skin in contact with the molten slag keeps thin. As the height of the ingot increases, the thickness of the slag skin near the solidified metal remains unchanged. Finally, a uniform slag skin is formed on the surface of the ingot.

Fig. 5 depicts the development of the melt pool profile with time. In Fig. 5(a), it is presumed that a 20 mm thick slag skin solidifies on the mold wall. As shown in Fig. 5(b), because the intense water cooling at the bottom of the mold, the floor of the melt basin is initially flat. As shown in Fig. 5(c), when the ingot expands, the effect of convective heat exchange at the bottom decreases and the depth of the melt basin increases. At the beginning, the heat of ingot is predominantly lost through the baseplate. Nonetheless, with the ingot expands, convective heat transfer becomes progressively more significant. As shown in Fig. 5(d), when the melt pool profile keeps

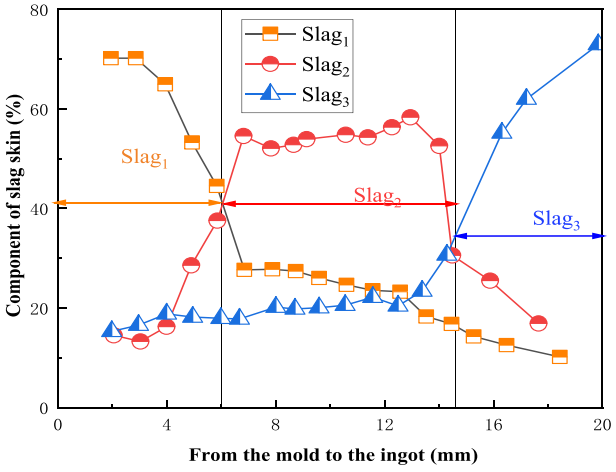

Fig. 6 – Distribution of slag skin composition (t = 150s).

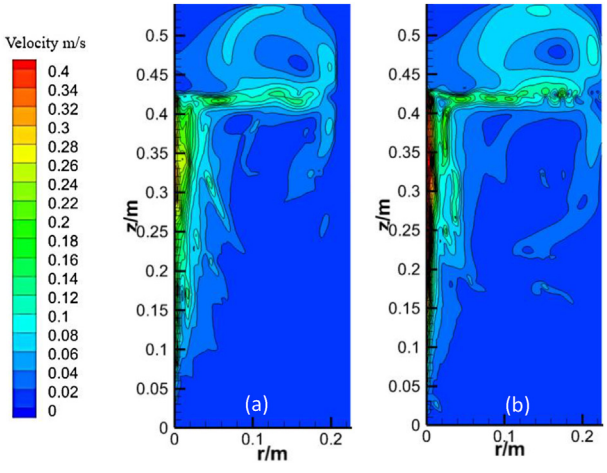

Fig. 7 – Velocity Distribution (a) with slag skin and (b) without slag skin.

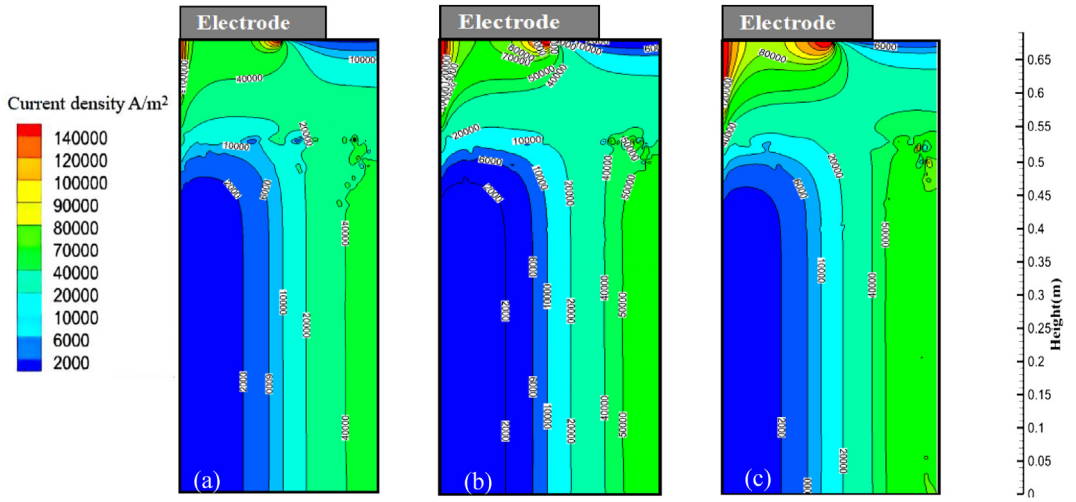

Fig. 8 – Current density distribution with (a) 2.0 kA (b) 2.5 kA and (c) 3.0 kA current.

unchange, it takes as a parabolic form. The distribution of slag skin composition at t = 150s is given in Fig. 6. As can be seen, three components of slag skin are distributed in layers due to the different solidification points of slag.

The majority of the flow within the mold consists of a Lorentz force-induced anticlockwise loop and a buoyancy-induced clockwise loop near the mold. Creating a clockwise cycle, the buoyancy-driven liquid metal flows horizontally, goes up along the front line of solidification of slag skin, and rotates to the centre. When the slag layer forms, the velocity near the wall is hindered. Fig. 7(a) shows that the slag remelting process with slag skin shows a significant gap at the mold in comparison to the slag remelting process without slag skin. The electromagnetic force has an axial component and a radial component [35]. The radial component makes the slag move in an axial direction, and the slag flows counterclockwise along the symmetrical axis, which is due to the pressure difference in the axial direction of the slag pool.

3.2. *Effect of current on slag skin solidification behavior*

Fig. 8 shows the current intensity distribution. The current enters from the electrode into the ingot and flows out of the bottom of ingot. Due to the different electrical conductivity of slag and metal, the current density will change. The majority of current flows at the corner of the electrode. When the current applied from 2 kA to 3 kA, the highest current density raised from $1.4 \times 10^5 A/m^2$ to $2.4 \times 10^5 A/m^2$. A slag skin is formed near the mold, which has the highest current intensity near the wall due to its lower electrical conductivity than the metal.

It can be observed from Fig. 9 that most of the Joule heating is produced at the electrode tip in the centre of the slag pool, and only minority of Joule heating are located in the other parts of slag pool. The distribution differences in Joule heating are beneficial to improve the melting rate and thermal efficiency of electrode. As the current or input power rise, the slag

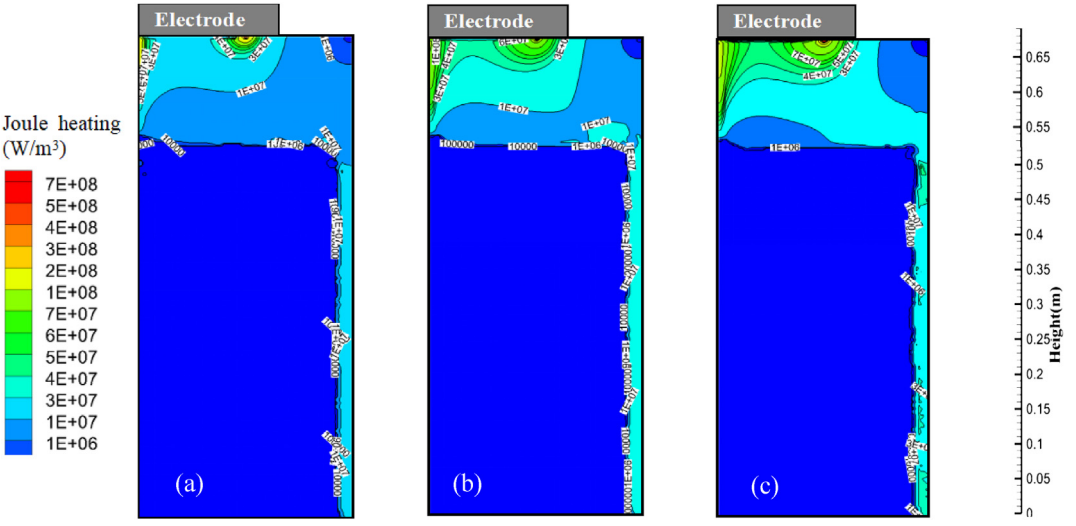

Fig. 9 – Joule heating distribution at main section with current (a) 2.0 kA (b) 2.5 kA and (c) 3.0 kA.

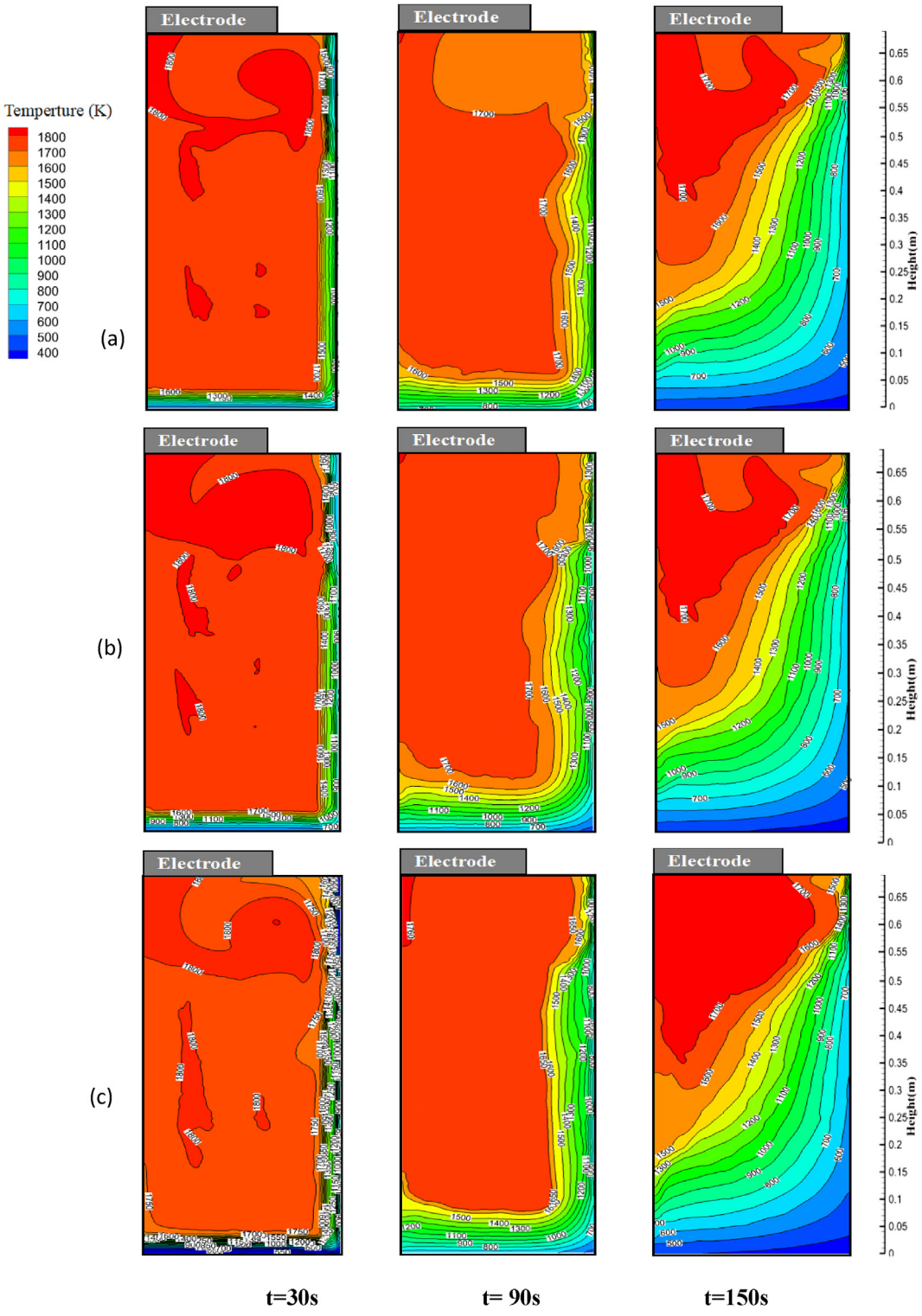

Fig. 10 – Temperature distribution versus time with (a) 2.0 kA, (b) 2.5 kA and (c) 3.0 kA current.

pool gets hotter as the Joule heating goes up. The highest amount of Joule energy changes from 1.3 × 10^9W/m^3 to 1.9 × 10^9W/m^3. The Joule heat spreads out in a horizontal direction, due to the presence of the slag skin, obtaining the maximum in the vicinity of the mold. The slag skin is not made of only single component, but a mixture of several components. Hence, there are different electrical conductivities of component.

The temperature distribution versus time is shown in Fig. 10. The highest temperature zone in a slag pool is approximately 1800 K, just located below the electrode. The side wall of slag pool has a large temperature gradient under

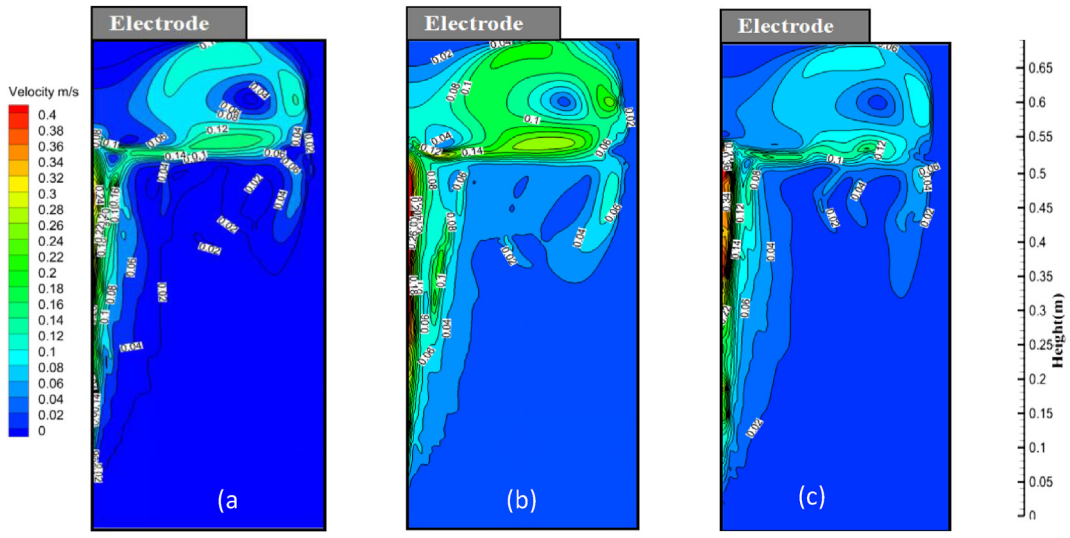

Fig. 11 – Velocity distribution versus current (t = 150s) (a) 2.0 kA, (b) 2.5 kA and (c) 3.0 kA.

the strong cooling capacity of mold. Since the flow at bottom of slag pool is weak, the temperature field shows obviously stratificated. As the current increases, the maximum temperature changes from 1800 K to 2200K. Due to the increasing applied current, the power, Joule heat and even the heat entering slag pool and metal pool also increased. In the meanwhile, the depth of slag pool and cooling capacity of mold remains same, hence the temperature increase. The increasing temperature causes an increment in thermal buoyancy, which accelerate the fluid flow in metal pool. The highest velocity increases from 0.22 to 0.35 m/s, as depicted in Fig. 11.

Variation of thickness of slag skin versus time at z = 0.46 m is listed in Fig. 12. When the current is 2.0 kA, the initial thickness of slag skin 20 mm is given at t = 0 s. When the current goes up to 2.0 kA, due to the low temperature of mold, the slag skin thickens to 22 mm. With the rising slag temperature, the thickness steadily lowers to 19 mm. Moreover,

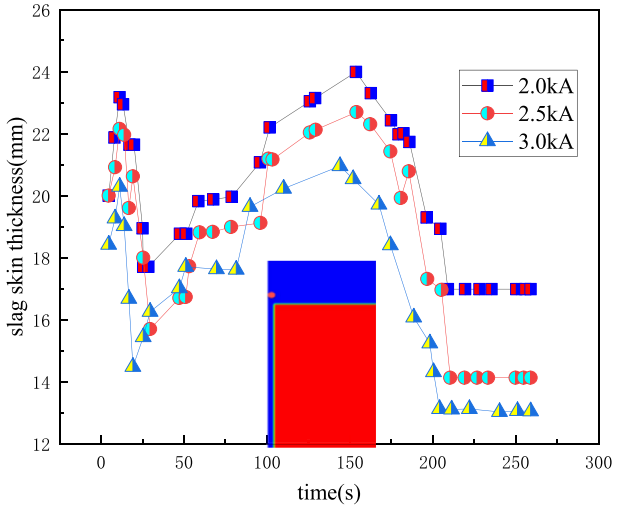

Fig. 12 – Variation of thickness of slag skin versus time at z = 0.46 m.

the thickness steadily increases to a highest of around 24 mm before entering the metallic pool. The thickness of slag skin is then partially remelted and reduced to 17 mm. Finally, a layer of slag skin 17 mm thick is spread evenly over the hardened ingot. As the current increases, the higher Joule heat and temperature in the slag skin are generated, which leads to the melting of the slag skin. When the current increase from 2.0 kA to 2.5 kA, the final slag thickness reduced from 17 mm to 13 mm.

The distribution of molten metal pools at various currents is shown in Fig. 13. With the rising current, the depth of pool of molten metal increases. This is because the increase in Joule heat with increasing current, which causes the temperature of the molten metal pool to rise. However, the cooling capacity of the water-cooled wall remains unaltered. As a result, the depth of molten metal pool deepens with the increase of applied current. In the ESR system, when the current increases from 2.0 kA to 3.0 kA, the current density, Joule heat, velocity, the pool of molten metal deepens and the thickness of the slag skin becomes thinner.

3.3. *Effect of vibrating electrode on slag skin solidification behavior*

Additionally, the research and analysis are done on how vibrating electrodes affect the behaviour of slag skin solidification during the ESR process, as depicted in Fig. 14.

In this paper, an electrode vibration test device is used to install a vibration source on the electrode holder, so that the electrode vibrates at a low speed during the ESR process. The relative motion between the electrode and the slag is enhanced due to the vibration of electrode, which accelerates the casting speed.

In Fig. 14 (a), it is evident that the droplets formed on the bottom surface of electrode without vibration are very scattered and unevenly distributed, and the droplet sizes are not the same. When the electrode is vibrating, the droplets formed at the bottom of electrode will converge to the center periodically and concentrate on the bottom surface when it

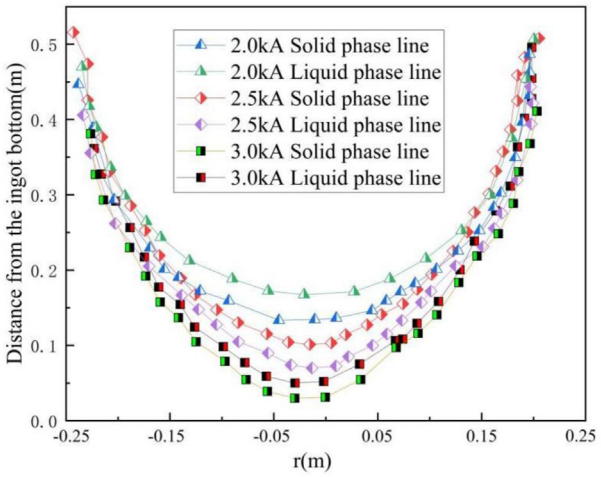

Fig. 13 – Melt metal pool distribution at different current.

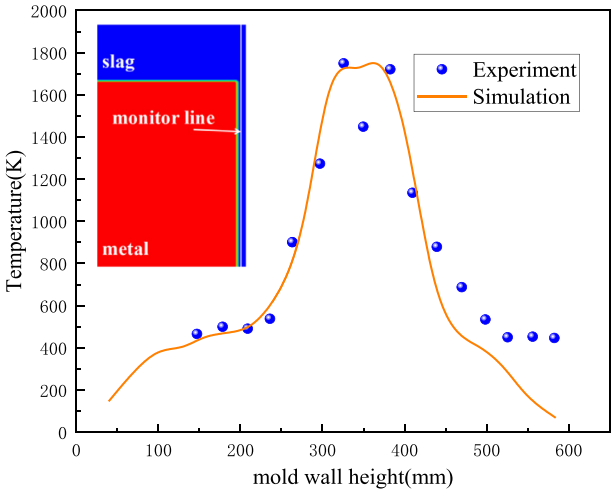

Fig. 15 – Variation of mold height versus temperature at t = 150s.

becomes a large enough droplet as shown in Fig. 13 (b). The electrode with or without vibration has no significant effect on the solidification melting and thickness of slag skin. Because the thickness of the slag skin is only related to the melting rate and the heat flux in mold, vibration electrode only affects the falling of metal droplet and the velocity field near the tip of the electrode in the layer of slag.

3.4. *Validation of thermodynamic model*

The same geometric and physical parameters, as well as the same operating settings in the experiment, were the same as in the simulated case. In this experiment, the temperature of mold was measured continuously. The thermocouple type WRN-191 is used and the temperature measurement module is the EM 231 (231-7PD22-0XA8) for the Simatic S7-200. A total of 18 thermocouples were involved in the experiment. The specification of thermocouples is Φ5 × 400 × 2000 mm. The external thread with M10 × 1 at the end of the thermocouple can be threaded with the mold copper tube. Firstly, a guide plate is laid on the bottom water tank and a mold is placed on it. The cooling water is passed into the mold before the electroslag remelt process starts, then the electrode is placed in the bottom centre of mold and inserted into the slag to a certain depth. Insert the thermocouple into the copper tube of mold modification, so that it is close to the inner wall of the mold and the power supply is turned on for melting and the temperature measurement data begins to record.

The variation of mold height versus temperature at t = 150s is shown in Fig. 15. A monitoring point is placed at R = 225 mm, which can record the variation of temperature at the monitoring point with time(height = 500 mm),depicted in Fig. 16. It is clear that the experimental values of the mold wall temperature are close to the simulated values, indicating that the established thermodynamic model is reasonable. The discrepancy was less than 5%, this variation can be attributed to uncertain physical characteristics of actual slag, heat contact resistance and thermal radiation.

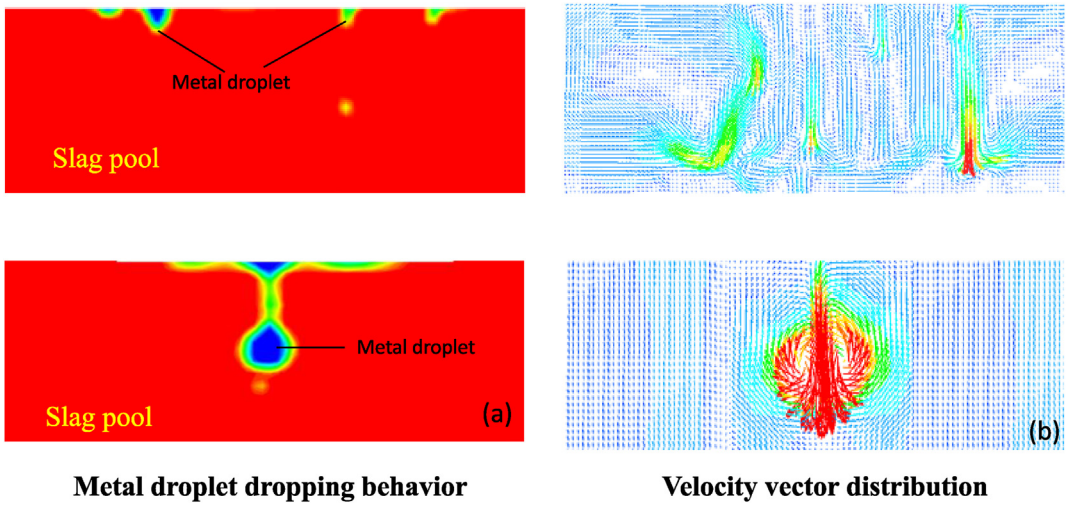

Fig. 14 – Metal droplet dropping behavior and velocity vector distribution with (a) Traditional ESR process and (b) ESR process with vibration electrode.

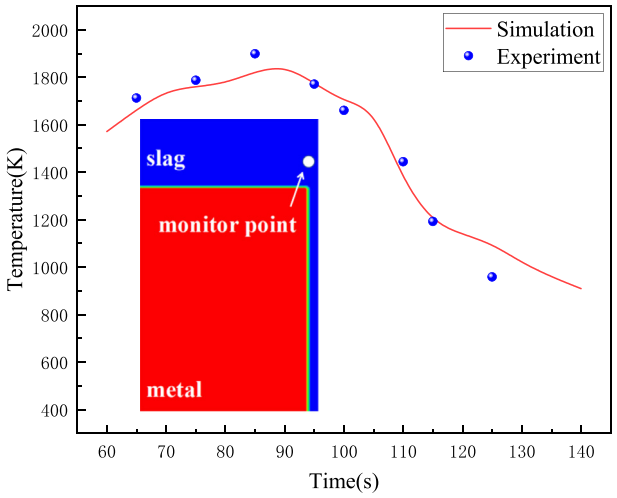

Fig. 16 – Variation of temperature versus time (height = 500 mm,R = 225 mm).

4. Conclusions

In this paper, the dynamic generation of slag skin in ESR process is studied by solving the Maxwell equations, Navier-Stokes equation and energy equation simultaneously. The developed model was proven to be reasonable through the experimental verification.

1. The slag skin thickness at the interface between slag skin and metal gets thicker as the axial distance from free surface of slag rises, reaching a maximum of about 25 mm. With the height of ingot increasing, the thickness of slag skin drops to 17 mm. At last, a consistent and very thin coating of slag skin is formed all over on the solidified ingot. Under the slag skin remelting, the ability of heat transfer mold effectively and continuously increases due to slag skin.
2. The height of the slag pool increases in proportion to the height of the ingot. In both the slag pool and the metal melt pool, there may be found three pairs of vortices.
3 The temperature gradient becomes lower as it varies from top to bottom along the radial direction, whereas, it gets lower as it travels from top to bottom along the axial direction.
4. The current increases from 2.0 kA to 3.0 kA, the current density, Joule heat, velocity and temperature in the remelting system increases, the slag skin becomes thinner and the melt pool becomes deeper.
5. The vibration of the electrode hardly has an impact on the slag skin, and only has effects on formation of metal dorplets driping and fluid flow in slag.

Declaration of competing interest

The authors declare that they have no known competing financial interests or personal relationships that could have appeared to influence the work reported in this paper.

Acknowledgments

This work was supported by the National Natural Science Foundation of China (No. 52171031), National Key Research and Development Program of China (No. 2022YFB3705101), Natural Science Foundation Plan of Liaoning Province (No. 2023010767-JH3/107).

List of symbols

$\vec{A}$	magnetic potential vector
A_{mush}	paste zone coefficient
b	reciprocal of Prandtl number
$\vec{B}$	magnetic flux density (T)
c_p	specific heat capacity ($J \cdot kg^{-1} \cdot K^{-1}$)
E	internal energy of mixed-phase concerning latent heat and temperature ($J \cdot kg^{-1}$)
f_1	liquid phase rate ($m \cdot s^{-1}$)
F_{st}	surface tension between slag and alloy phase ($N \cdot m^{-3}$)
F_e	Lorentz force (N)
F_d	paste zone resistance (N)
F_t	thermal buoyancy force due to density difference ($N \cdot m^{-3}$)
F_c	electromagnetic force ($N \cdot m^{-3}$)
F_t	resistance of mushy zone ($N \cdot m^{-3}$)
h_r	radiative heat transfer coefficients of air gap ($W \cdot (m^{-1}K^{-1})$
h_c	convective heat transfer coefficients of air gap ($W \cdot (m^{-1}K^{-1})$
h_w	total heat transfer coefficient between metal and cooling water ($W \cdot (m^{-1}K^{-1})$
$\vec{H}$	magnetic field strength ($A \cdot m^{-1}$)
$\vec{J}$	current density ($A \cdot m^{-2}$)
k_{eff}	effective thermal conductivity ($W \cdot (m^{-1}K^{-1})$
k	turbulent kinetic energy ($m \cdot s^{-1}$)
k_s	thermal conductivity of slag skin ($W \cdot (m^{-1}K^{-1})$
k_m	thermal conductivity of mold ($W \cdot (m^{-1}K^{-1})$
L	latent heat of melting ($J \cdot kg^{-1}$)
Q_J	Joule heat ($W \cdot m^{-3}$)
$R_{contact}$	contact thermal resistance ($W \cdot (m^{-1}K^{-1})$
t	Time (s)
T_1	liquid phase line temperatures of metal (K)
T_s	solid phase line temperatures of metal (K)
v_{cast}	casting velocity ($m \cdot s^{-1}$)

Greek symbols

α_i	volume fractions. The subscript i represents the type of substance, including metal(m), liquid slag(s), solid slag1(s1),solid slag2(s2) and solid slag3(s3)
μ_0	magnetic permeability of medium ($F \cdot m^{-1}$)
μ	laminar viscosity ($Pa \cdot s$)
$\overline{\rho}$	density of mixed-phase ($kg \cdot m^{-3}$)
ρ_m	densities of metal ($kg \cdot m^{-3}$)
$\overline{\rho_s}$	densities of mixed-slag phase ($kg \cdot m^{-3}$)
σ	conductivity of magnetic fluid ($\Omega^{-1} \cdot m^{-1}$)
$\overline{\varphi}$	mixed-phase parameter
$\overline{\varphi}_m$	parameters of metal phase
$\overline{\varphi}_s$	parameters of liquid slag phase

ϑ_i	volume fractions
ε	dissipation rate
δs	thickness of slag skin (mm)
δm	thickness of mold (mm)

REFERENCES

[1] Li ZB. Development of electroslag metallurgy and casting in China. China Foundry 2004;1:7–16. https://doi.org/10.3321/j.issn:1001-4977.2004.11.001.

[2] Ludwig A, Kharicha A, Wu M. Modeling of multiscale and multiphase phenomena in materials processing. Metall Mater Trans B 2014;45:36–43. https://doi.org/10.1007/s11663-013-9820-1.

[3] Boye H, Staate Y, Schmidt J. Experimental investigation and modelling of heat transfer during convective boiling in a minichannel. Int J Heat Mass Transf 2007;50:208–15. https://doi.org/10.1016/j.ijheatmasstransfer.2006.06.017.

[4] Wang Q, Wang F, Li G, Gao Y, Li B. Simulation and experimental studies of effect of current on oxygen transfer in electroslag remelting process. Int J Heat Mass Transf 2017;113:1021–30. https://doi.org/10.1016/j.ijheatmasstransfer.2017.06.007.

[5] Bacon G, Mitchell A, Nishizaki RM. Electroslag remelting with all-fluoride low conductivity slags. Metall Mater Trans B 1972;3:631–5. https://doi.org/10.1007/BF02642744.

[6] Li F, Fu R, Feng D, Yin F, Tian Z. Microstructure and segregation behavior of rene88dt alloy prepared by esr-cds. Rare Metal Mat Eng 2016;45:1437–42. https://doi.org/10.1016/S1875-5372(16)30127-8.

[7] Wang F, Tan JP, Huang XC, Wang Q, Liu ZQ, Baleta J, et al. Mathematical and numerical predictions of desulfurization behavior in the electromagnetically controlled vibrating-electrode electroslag remelting furnace. Metal Materials Trans B, Process Metal Materials Process Sci 2022;53:1792–805. https://doi.org/10.1007/s11663-022-02487-5.

[8] Li ZB. Theory and practice of electroslag metallurgy. first ed. Beijing: Metallurgical Industry Press; 2010.

[9] Li Q, Xia Z, Guo Y, Shen Z, Zheng T, Zhong Y. Microstructure evolution and mechanical properties improvement in magnetic-controlled electroslag remelted bearing steel. ISIJ Int 2020;60:2462–70. https://doi.org/10.2355/isijinternational.ISIJINT-2020-173.

[10] Zhang GG, Hu Y, Hou D, Yang D, Zhang Q, Hu Y, et al. Assessment of porosity defects in ingot using machine learning methods during electro slag remelting process. Metals 2022;12:958. https://doi.org/10.3390/met12060958.

[11] Yu J, Jiang ZH, Liu F, Chen K, Li H, Geng X. Effects of metal droplets on electromagnetic field, fluid flow and temperature field in electroslag remelting process. ISIJ Int 2017;57:1205–12. https://doi.org/10.2355/isijinternational.ISIJINT-2017-084.

[12] Zhao JX, Chen Y, Li X, Cui Y, Lu X. Mechanism of slag composition change during electroslag remelting process. J Iron Steel Res Int 2011;18:24–8.

[13] Yu J, Liu FB, Li H, Jiang ZH, Chen K, Geng X. Effects of mold current on slag skin and heat flow distribution during electroslag remelting at given power input. Jom 2019;71:744–53. https://doi.org/10.1007/s11837-018-3276-3. 1989.

[14] Hugo M, Dussoubs B, Jardy A, Escaffre J, Poisson H. Influence of the mold current on the electroslag remelting process. Metal Materials Trans B, Process Metal Materials Process Sci 2016;47:2607–22. https://doi.org/10.1007/s11663-016-0694-x.

[15] Yanke J, Fezi K, Trice RW, Krane MJM. Simulation of slag-skin formation in electroslag remelting using a volume-of-fluid method. Numerical heat transfer. Part A, Applications 2015;67:268–92. https://doi.org/10.1080/10407782.2014.937208.

[16] Yu J, Liu F, Jiang Z, Kang C, Chen K, Li H, et al. Numerical simulation of the dynamic formation of slag skin and heat flow distribution during the electroslag remelting process. Steel Res Int 2018;89:1700481. https://doi.org/10.1002/srin.201700481.

[17] Kharicha A, Schützenhöfer W, Ludwig A, Tanzer R, Wu M. On the importance of electric currents flowing directly into the mold during an esr process. Steel Res Int 2008;79:632–6. https://doi.org/10.1002/srin.200806176.

[18] Meng Q, Xu L, Niu R. Mechanism study of esr ingot slag skin. J Mater Metall 2012;11:265–7.

[19] Li YB, Zhao JX, Tang WD, Dang YM, Qiu ST, Cui YR. Composition and structure of slag shell during electroslag remelting process with caf2-al2o3-cao slag series. Spec Steel 2014;35:28–30.

[20] Zhao J, Ge B, Liu S, Tang W, Li X, Qiu S. Relation between slag skin and slag pool on structure and composition in esr process. Chinese Journal of Engineering 2016;38:155–9. https://doi.org/10.13374/j.issn2095-9389.2016.s1.026.

[21] Chu SJ, Liu HH, Duan SS, Su QY. Characterization of solidification of esr ingot slag skin. Eng Chem Metal 1992:111–7.

[22] Feng L, Shi W. The influence of eddy effect of coils on flow and temperature fields of molten droplet in electromagnetic levitation device. Metal Materials Trans B, Process Metal Materials Process Sci 2015;46:1895–901. https://doi.org/10.1007/s11663-015-0360-8.

[23] Kharicha A, Ludwig A, Wu M. On melting of electrodes during electro-slag remelting. ISIJ Int 2014;54:1621–8. https://doi.org/10.2355/isijinternational.54.1621.

[24] Wang Q, Zhao R, Fafard M, Li B. Three-dimensional magnetohydrodynamic two-phase flow and heat transfer analysis in electroslag remelting process. Appl Therm Eng 2015;80:178–86. 10.1016/j.applthermaleng.2014.12.075.

[25] Li B, Wang B, Tsukihashi F. Modeling of electromagnetic field and liquid metal pool shape in an electroslag remelting process with two series-connected electrodes. Metal Materials Trans B, Process Metal Materials Process Sci 2014;45:1122–32. https://doi.org/10.1007/s11663-013-9996-4.

[26] Wang Q, Li B. Numerical investigation on the effect of fill ratio on macrosegregation in electroslag remelting ingot. Appl Therm Eng 2015;91:116–25. https://doi.org/10.1016/j.applthermaleng.2015.08.013.

[27] Schneider MC, Beckermann C. Formation of macrosegregation by multicomponent thermosolutal convection during the solidification of steel. Metall Mater Trans A 1995;26:2373–88. https://doi.org/10.1007/BF02671251.

[28] Sun H, Zhang J. Study on the macrosegregation behavior for the bloom continuous casting: model development and validation. Metal Materials Trans B, Process Metal Materials Process Sci 2014;45:1133–49. https://doi.org/10.1007/s11663-013-9986-6.

[29] Fezi K, Yanke J, Krane MJM. Macrosegregation during electroslag remelting of alloy 625. Metall Mater Trans B 2015;46:766–79. https://doi.org/10.1007/s11663-014-0254-1.

[30] Wang Q, Rong W, Li B. Effect of power control function on heat transfer and magnetohydrodynamic two-phase flow in electroslag remelting furnace. JOM 2015;67:2705–13. https://doi.org/10.1007/s11837-015-1621-3. 1989.

[31] H MW. Heat transmission. first ed. New York: McGraw-Hill book Company; 1988.
[32] Mitchell A, Joshi S. The thermal characteristics of the electroslag process. Metall Trans A 1973;4:631–42. https://doi.org/10.1007/BF02643068.
[33] Weber V, Jardy A, Dussoubs B, Ablitzer D, Rybéron S, Schmitt V, et al. A comprehensive model of the electroslag remelting process: description and validation. Metal Materials Trans B, Process Metal Materials Process Sci 2009;40:271–80. https://doi.org/10.1007/s11663-008-9208-9.
[34] Jiang Z. Physical chemistry and transport phenomena during electroslag metallurgy. Shenyang: Northeastern University Press; 2000.
[35] Wang Q, Jia S, Qi F, Li G, Li Y, Wang T, et al. A cfd study on refractory wear in rh degassing process. ISIJ Int 2020;60:1938–47. https://doi.org/10.2355/isijinternational.ISIJINT-2019-768.